



External Inertia Emulation to Facilitate Active-Power Limitation in Grid-Forming Converters

Downloaded from: <https://research.chalmers.se>, 2025-09-25 15:36 UTC






Citation for the original published paper (version of record):

Imgart, P., Narula, A., Bongiorno, M. et al (2024). External Inertia Emulation to Facilitate Active-Power Limitation in Grid-Forming Converters. IEEE Transactions on Industry Applications, 60(6): 9145-9156. <http://dx.doi.org/10.1109/TIA.2024.3443792>

N.B. When citing this work, cite the original published paper.

© 2024 IEEE. Personal use of this material is permitted. Permission from IEEE must be obtained for all other uses, in any current or future media, including reprinting/republishing this material for advertising or promotional purposes, or reuse of any copyrighted component of this work in other works.

External Inertia Emulation to Facilitate Active-Power Limitation in Grid-Forming Converters

Paul Imgart , *Graduate Student Member, IEEE*, Anant Narula , *Member, IEEE*,
Massimo Bongiorno , *Senior Member, IEEE*, Mebtu Beza , *Member, IEEE*,
and Jan R. Svensson , *Senior Member, IEEE*

Abstract—The aim of this paper is to present a grid-forming (GFM) control strategy with a novel active-power loop (APL) structure facilitating limitation of active power while providing maximum available inertial support. This is achieved by decoupling the synchronization duties of the APL from the inertial support. The latter is provided by calculating the active-power reference through a dedicated inertia-emulation loop (IEL), which is connected in cascade with the APL. The effectiveness of the proposed method is demonstrated through laboratory experiments including frequency transients of varying size and unbalanced operating conditions.

Index Terms—Current limiting, frequency stability, grid-forming converter, grid-connected converter, inertia, low-inertia power system, rate of change of frequency.

I. INTRODUCTION

WORLD-WIDE transformation efforts towards the future renewable-based power system result in the replacement of synchronous with converter-interfaced generation. The preferred solution for the challenges associated with this development are grid-forming (GFM) converters, which typically rely on their active-power loop (APL) for grid synchronization [1]. This allows the converter to act as a voltage source and enables to easily provide a number of ancillary services such as inertial support and fault current contribution [2]. One of the main challenges for GFM converters is the necessity to limit the converter current and at the same time maintain stable operation and the required GFM properties [3]. Due to this, as reviewed

recently in [4] a large number of publications is available on the topic of current limitation in GFM converters. The vast number of current-limitation strategies for GFM converters can be sorted into three main categories [4]: strategies employing a type of current-reference limiter such as [5], [6], [7], [8], [9], strategies relying on a virtual impedance for current limitation as for example [10], [11], and finally strategies employing a limitation of the virtual back electro-motive force (EMF) such as [12]. The referenced articles as well as the majority of existing studies dealing with the stability of current-limited GFM converters [6], [13], [14] focus on current limitation during voltage dips. However, as this article will show, grid-frequency disturbances are a relevant cause of current saturation that can lead to angular instability. This kind of disturbance is particularly challenging when the APL provides not only grid synchronization, but also inertial support.

From the few available publications dealing with frequency-disturbance induced instability, mainly three types of current limitation strategies have been identified. The first is control-mode switching (CMS), as suggested e.g. in [15], where a complex modified droop control manipulates the active and reactive power references based on the converter currents to prevent loss of synchronism due to current saturation. A different approach involving CMS is presented in [16], selecting different frequency-response strategies based on frequency deviation and an estimate of the rate of change of frequency (RoCoF). A third example is given in [17], where a re-synchronization aid function is employed to limit frequency variation while the converter is in current control mode. The second type of strategy is to adapt the inertia, which in [18] is based on grid impedance estimation, to ensure a chosen stability margin for the GFM converter. The third strategy is to switch the synchronization duty during current limitation to a backup synchronization unit, typically a phase-locked loop (PLL) [19], [20], [21].

CMS as well as parameter adaptation change the converter's properties abruptly, which is typically not desirable. Furthermore, some implementations require knowledge of system parameters such as the grid impedance, which is typically unknown. Inaccurate estimation of these parameters results in either too conservative or excessive limits, making it challenging to fully utilize the converter's actual capabilities without risk of overcurrent [22]. Furthermore, these solutions are typically tailor-made for a specific GFM controller, resulting in a challenging adaptation for usage with other control strategies. The

Manuscript received 30 August 2023; revised 13 December 2023, 6 March 2024, and 18 May 2024; accepted 25 June 2024. Date of publication 15 August 2024; date of current version 15 November 2024. Paper 2023-PEDCC-0732.R3, presented at the 2022 IEEE Energy Conversion Congress and Exposition, Detroit, MI, USA, Oct. 09–13, and approved for publication in the IEEE TRANSACTIONS ON INDUSTRY APPLICATIONS by the Power Electronic Devices and Components Committee of the IEEE Industry Applications Society [DOI: 10.1109/ECCE50734.2022.9947721]. This work was supported by the Energimyndigheten, Svenska Kraftnät and Hitachi Energy. (Corresponding author: Paul Imgart.)

Paul Imgart, Anant Narula, Massimo Bongiorno, and Mebtu Beza are with the Division of Electric Power Engineering, Chalmers University of Technology, 412 96 Göteborg, Sweden (e-mail: paul.imgart@chalmers.se; anant.narula@chalmers.se; massimo.bongiorno@chalmers.se; mebtu.beza@chalmers.se).

Jan R. Svensson is with the Hitachi Energy Research, Hitachi Energy, 722 26 Västerås, Sweden (e-mail: jan.r.svensson@hitachienergy.com).

Color versions of one or more figures in this article are available at <https://doi.org/10.1109/TIA.2024.3443792>.

Digital Object Identifier 10.1109/TIA.2024.3443792

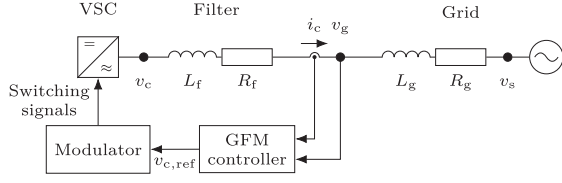


Fig. 1. Circuit diagram and control system of a grid-connected converter.

use of a backup PLL during current saturation changes the controller's characteristics and, depending on the implementation, can result in the loss of some of the converter's GFM capabilities [23], which is undesirable as they are typically needed the most during grid disturbances.

The aim of this article is to propose a solution to the GFM stability problem by decoupling the synchronization task of the APL from the provision of inertia. To address the issue properly, the root causes of angular instability in GFM converters are investigated. Here, the focus lies on the sources of instability for inertia-providing controllers in case of large grid-frequency disturbances. It is shown that existing solutions available in the literature, typically based on variation of the active-power reference [5], [6], [10], [13], [14], are not effective for this kind of event because the inertial effect appears in the APL after the reference variation. Based on this analysis, a new solution originally presented in [24] is investigated, consisting of an inertia-emulation loop (IEL) in cascade with a fast APL. The IEL is based on the structure of a PLL and is used to generate an active-power reference emulating the desired amount of inertia, whereas the APL provides synchronization with the grid. Decoupling the synchronization loop from the inertia provision enables to dynamically limit the converter's load angle through the limitation of the active-power reference. As a consequence, the current output of the converter can always be controlled within the converter's ratings without the need for a current-reference limiter, thus preventing instability due to grid-frequency disturbances [25], [26]. Next, the tuning procedure for APL and IEL is established, demonstrating how the IEL parameters relate to the desired inertia constant and damping ratio of the inertial response. This is followed by experimental validation, demonstrating that the desired behavior is achieved. Thanks to the proposed control strategy, it is possible to preserve the GFM properties and limit the converter current without the need for control-mode switching or parameter adaptation.

II. GRID-FORMING CONVERTER STABILITY PROBLEM

The common property of the majority of the GFM control structures suggested in the literature is that the converter should be modelled as a voltage source behind an impedance [2], [27]. This behavior can be achieved using different grid-synchronization methods, e.g. using a dedicated synchronization unit like a PLL. Fig. 1 shows a typical grid-connected converter with its controller and the control input and output signals. GFM converters typically synchronize by relying on the active-power transfer, which can provide increased robustness in weak grids

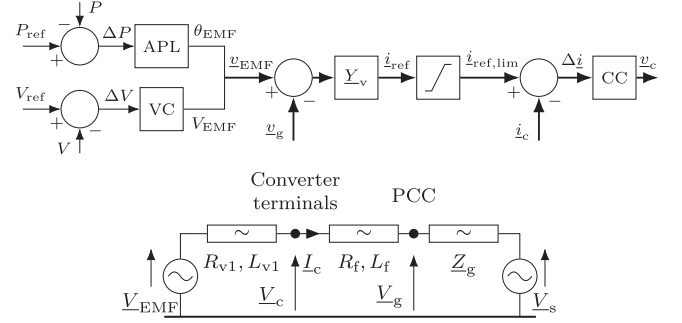


Fig. 2. Block scheme (top) and equivalent circuit (bottom) representation of the virtual admittance-based GFM control approach.

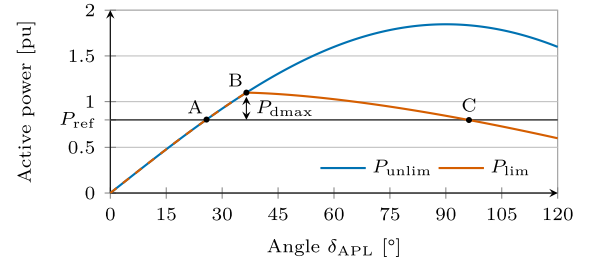


Fig. 3. P - δ_{APL} curve illustrating the converter angle stability problem for a current limit of 1.1 pu with $V_g = 1$ pu. A: Pre-disturbance operating point; B: Current limit reached; C: transient stability limit; P_{dmax} : maximum decelerating power.

and islanding operation [28]. In this work, the virtual admittance-based approach from [29] is implemented with the structure displayed in Fig. 2. A detailed description of the control system follows in the next section, as the results of this study are not specific for this control structure.

Angle instability in GFM converters mainly occurs due to two reasons: firstly, the power reference being too large for the grid conditions such as grid strength and voltage, e.g. during a fault [5], [6], [10], [13], [14]; secondly, the power controller being unable to follow the grid voltage angle in case of an angle jump or frequency disturbance. The latter is the focus of this paper.

For the system depicted in Fig. 2 (bottom figure), neglecting the system losses the steady state per-unit converter current is

$$\underline{I}_c = \frac{\underline{V}_{EMF} - \underline{V}_s}{jX} = \frac{V_s \sin \delta + j(V_s \cos \delta - V_{EMF})}{X}, \quad (1)$$

where the dq -frame is aligned with the converter back EMF, δ denotes the phase displacement between \underline{V}_{EMF} and \underline{V}_s , and X is the sum of reactances between them¹. The active-power transfer from the converter to the grid is defined with $*$ symbolizing the complex conjugate as

$$P = \Re \{ \underline{V}_{EMF} \underline{I}_c^* \} = \frac{V_s V_{EMF}}{X} \sin \delta, \quad (2)$$

and shown in blue in Fig. 3 for an example system.

¹The virtual admittance $\underline{Y}_v = \underline{Z}_v^{-1}$ in Fig. 2 is the inverse of the series of the virtual impedance \underline{Z}_{v1} and the physical filter impedance \underline{Z}_f .

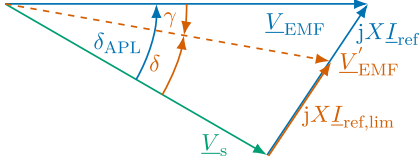


Fig. 4. Phasor diagram illustrating the effect of current limitation on the virtual back EMF. Unlimited in blue, limited in red.

Denoting with I_{\max} the maximum allowed converter current and using circular current limitation [5] on the current reference I_{ref} , the limited converter-current reference is

$$I_{\text{ref,lim}} = I_{\text{ref}} \frac{I_{\max}}{I_{\text{ref}}} \quad \forall I_{\text{ref}} > I_{\max}. \quad (3)$$

Note that the activation of the current limiter is equivalent to a variation of the phasor V_{EMF} , defined as V'_{EMF} in Fig. 4. From the figure, current limitation results in a reduction of the load angle δ when compared with the unlimited case, denoted as δ_{APL} . Even despite this reduction, the angle δ_{APL} still has an impact on the exchanged active power, as it determines the angle of the current reference I_{ref} . Using (1)-(3), the relation between δ_{APL} and the current-limited active power P_{lim} is given as

$$\begin{aligned} P_{\text{lim}} &= \Re\{V_s I_{\text{ref,lim}}^*\} \\ &= V_s V_{\text{EMF}} \sin \delta_{\text{APL}} \frac{I_{\max}}{\sqrt{V_s^2 + V_{\text{EMF}}^2 - 2V_s V_{\text{EMF}} \cos \delta_{\text{APL}}}}, \\ &\quad \forall I_{\text{ref}} > I_{\max}. \end{aligned} \quad (4)$$

Fig. 3 illustrates the current-limited P - δ_{APL} relationship following from (4) in red. After the current saturates at B, the power transfer decreases for increasing δ_{APL} .

The type of instability highlighted in this section is caused by an inability of inertia-providing APLs to follow the grid voltage angle in case of severe frequency disturbances or phase angle jumps. To follow a change in the grid frequency, the APL needs to adapt its internal frequency, which requires a power control error. As an example, a frequency decline would cause the load angle δ to increase until the additional decelerating power $P_d = -2H \frac{d\omega_g}{dt}$ is achieved, where H is the APL's inertia constant in s and ω_g is the grid-voltage angular frequency in rad/s. This decelerating power will appear as a steady-state error in the active power for a constant RoCoF. When the current is limited, the needed decelerating power might not be reached, resulting in an continuously increasing load angle. This can cause the loss of synchronism if the unstable equilibrium point C is passed, equivalent to first swing instability in a synchronous machine (SM). It should be noted that the decelerating power only depends on the APL's control parameters and the grid disturbance, not on the active power reference. It is therefore impossible to affect this power control error by limiting the reference, and even during operation with an active-power reference of zero the decelerating power can cause the converter's current limiter to saturate for large inertia constants and frequency disturbances.

The simulation shown in Fig. 5 illustrates this instability mechanism caused by a frequency decrease. During unsaturated

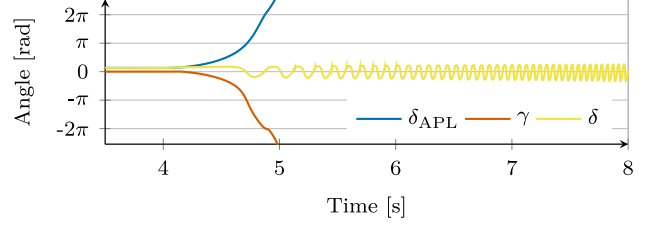


Fig. 5. δ_{APL} , γ and δ for converter instability due to frequency disturbance at 4 s.

operation, the angle γ defined in Fig. 4 is zero. During limitation, the required deceleration power P_d cannot be reached and the APL angle δ_{APL} increases steadily. As a consequence, γ is decreasing at an accelerating rate, which demonstrates the loss of the synchronization signal. In this case, loss of synchronism cannot be prevented by limiting the active-power reference, because the additional power is not caused by a change in reference, but by the APL's inability to reject the grid disturbance. GFM converters are prone to this type of instability when they rely on the active-power transfer for synchronization. Due to this, the APL output is not a load angle, but a ramp-formed phase angle. When the APL angle output is manipulated to guarantee current limitation, the synchronization signal is lost. Large inertia, high RoCoF and operating points close to the maximum power transfer will increase the risk for this kind of instability, as the necessary decelerating power increases or the available current for decelerating power decreases, respectively.

III. PROPOSED SOLUTION

The GFM design incorporating both synchronization and inertial response in the APL is the approach typically encountered in the literature for GFM converters providing an inertial response [28], and will here be referred to as *integrated GFM*. To overcome the described risk for instability present in these approaches, the cascaded structure for the converter's active-power controller displayed in Fig. 6 is proposed here. The PI-based APL tracks the active-power reference and synchronizes with the grid by generating the angle for the converter virtual back EMF. As the duty of the APL is to provide synchronization only, a relatively high loop bandwidth can be selected to ensure good dynamic performance regarding both disturbance rejection (e.g. in the case of phase jumps) and reference tracking.

The inertia response P_H is instead calculated by the IEL and added onto the APL's power reference P_{set} . This is similar to the approaches proposed in [30], [31], where a PLL is used to provide an inertial response from a grid-following converter. The advantage of the proposed approach over other methods to provide RoCoF-proportional inertial response is that the frequency derivative is implicitly determined within the IEL. This replaces the noise-sensitive derivation step and means that the RoCoF estimate is immediately available, reducing delays in the converter's inertial response [30]. By generating the inertial response explicitly as a part of the power reference, it can be effectively limited, preventing the previously described instability. In the integrated GFM, a large frequency

An ongoing grid-frequency disturbance will however result in a steady-state error in the active power, similar to an inertial response. This can be shown by examining the transfer function from a change the grid voltage angle θ_g to the change in the active power ΔP ,

$$G_g(s) = \frac{\Delta P}{\Delta \theta_g} = \frac{-s^2}{P_{\text{vmax}}^{-1}s^2 + (K_{\text{pPC}} + K_{\text{pd}})s + K_{\text{iPC}}}. \quad (7)$$

A constant RoCoF can be expressed by $\Delta \theta_g = \frac{k\omega_b}{s^3}$, where k is the RoCoF in pu and ω_b is the base angular frequency in rad/s. The steady-state error is then given by applying the final value theorem:

$$\lim_{t \rightarrow \infty} \Delta P = \lim_{s \rightarrow 0} s G_g(s) \frac{k\omega_b}{s^3} = -\frac{k\omega_b}{K_{\text{iPC}}}. \quad (8)$$

If desired, inertial contribution from the APL under the presence of a constant RoCoF can be removed by adding a second-order integrator. In this case, an integrative gain has to be included in the active-damping term to achieve the desired control behavior. This corresponds to the APL shown in Fig. 6 including the blocks in red. The tuning of this second-order APL follows the same loop-shaping approach and is shown below.

The active-power transfer from the converter to the grid neglecting resistances is given by the two port (2), which can be applied here due to the relatively slow speed of APLs, allowing to use quasi-steady state equations. To tune the controller properly, the equation is formulated with regard to the measurable PCC voltage instead of the Thévenin source, with $\delta = \theta_{\text{EMF}} - \theta_g$. Linearizing this equation for small angle differences, and formulating the transfer function for a change in the converter angle with a constant grid voltage phase angle gives the plant model for the controller design as

$$G_\theta(s) = \frac{\Delta P}{\Delta \theta_{\text{EMF}}} = \frac{V_{\text{EMF}} V_g}{X_V} = P_{\text{vmax}}. \quad (9)$$

The closed-loop transfer function for a step in the power reference including the controller and plant model contains a first- and second-order zero, which results in a pronounced overshoot in the step response. To remove this overshoot, the active damping terms K_{pd} and K_{id}/s are introduced as displayed in Fig. 6. This is similar to the approach typically used for vector current controllers (e.g. as suggested in [35]), but in this case an integrative term is included in the active damping as well to cancel the second-order zero. This results in the transfer function from the output of the PI-regulator to the injected active power

$$G_\omega(s) = \frac{\Delta P}{\Delta \omega_c} = \frac{1}{K_{\text{id}}} \frac{P_{\text{vmax}} K_{\text{id}} s}{s^2 + P_{\text{vmax}} K_{\text{pd}} s + P_{\text{vmax}} K_{\text{id}}}, \quad (10)$$

which corresponds to a second-order system with natural frequency $\omega_0 = \sqrt{P_{\text{vmax}} K_{\text{id}}}$ and the damping ratio $\zeta_D = P_{\text{vmax}} K_{\text{pd}} (2\omega_0)^{-1}$. Good results have been achieved by selecting the natural frequency to match half of the desired control-loop bandwidth α_{PC} , and choosing a damping ratio of 2, which results in

$$K_{\text{id}} = \frac{\omega_0^2}{P_{\text{vmax}}} = \frac{\alpha_{\text{PC}}^2}{4P_{\text{vmax}}} \quad \text{and}$$

$$K_{\text{pd}} = \frac{2\omega_0 \zeta_D}{P_{\text{vmax}}} = \frac{2\alpha_{\text{PC}}}{P_{\text{vmax}}}. \quad (11)$$

The closed-loop transfer function from the reference to the actual active power is

$$G_{\text{PC}}(s) = \frac{\Delta P}{\Delta P_{\text{ref}}} = \frac{P_{\text{vmax}} F_{\text{PC}}}{s + P_{\text{vmax}} (F_{\text{PC}} + F_{\text{D}})}, \quad (12)$$

with

$$F_{\text{PC}} = K_{\text{pPC}} + \frac{K_{\text{iPC}}}{s} + \frac{K_{\text{sPC}}}{s^2} \quad \text{and} \quad F_{\text{D}} = K_{\text{pd}} + \frac{K_{\text{id}}}{s}. \quad (13)$$

A proper selection of the controller gains by comparing coefficient reduces the system order to one:

$$G_{\text{PC}}(s) = \frac{P_{\text{vmax}} F_{\text{PC}}}{s + P_{\text{vmax}} (F_{\text{PC}} + F_{\text{D}})} = \frac{\alpha_{\text{PC}}}{s + \alpha_{\text{PC}}}, \quad (14)$$

with

$$\frac{s}{\alpha_{\text{PC}}} = \frac{s + P_{\text{vmax}} F_{\text{D}}}{P_{\text{max}} F_{\text{PC}}} \quad (15)$$

resulting in

$$F_{\text{D}} = F_{\text{PC}} \frac{s}{\alpha_{\text{PC}}} - \frac{s}{P_{\text{vmax}}} \quad (16)$$

and finally in

$$K_{\text{pd}} + \frac{K_{\text{id}}}{s} = K_{\text{pPC}} \frac{s}{\alpha_{\text{PC}}} + \frac{K_{\text{iPC}}}{\alpha_{\text{PC}}} + \frac{K_{\text{sPC}}}{\alpha_{\text{PC}} s} - \frac{s}{P_{\text{vmax}}}. \quad (17)$$

This yields the controller gains

$$\begin{aligned} K_{\text{pPC}} &= \frac{\alpha_{\text{PC}}}{P_{\text{vmax}}} \\ K_{\text{iPC}} &= \alpha_{\text{PC}} K_{\text{pd}} = \frac{2\alpha_{\text{PC}}^2}{P_{\text{vmax}}} \\ K_{\text{sPC}} &= \alpha_{\text{PC}} K_{\text{id}} = \frac{\alpha_{\text{PC}}^3}{4P_{\text{vmax}}}. \end{aligned} \quad (18)$$

As mentioned before, the addition of a second-order integrator in the APL is optional with the aim to reduce the amount of inertial response from the APL. If a first-order controller is preferred, setting the parameters K_{sPC} and K_{id} in (11) and (18) to 0 results in the same parameter values as (5).

Since in the proposed controller the IEL provides the inertial response and the APL is only responsible for power reference tracking and synchronization, the bandwidth α_{PC} can be selected as desired. Advantages of a fast APL include better rejection of grid-frequency disturbances and consequently more robust synchronization as well as better power reference tracking. In this publication, an APL loop bandwidth of 5 Hz is chosen, which is in the frequency range typical used in PLLs used for synchronization in grid-following converters while still respecting the upper limit for control-loop bandwidths for GFM control from the grid codes reported in [36].

B. Inertia-Emulation Loop Tuning

The IEL is tuned to behave equivalent in terms of inertial power contribution to a SM. The IEL's output is the pure inertial

response P_H , which is equivalent to a lossless synchronous condenser (SC), where the mechanical power $P_m = 0$. The fundamental idea is that both SC and IEL track the phase angle of the grid voltage with a given speed, which corresponds to their inertia.

The relation between a change in rotor speed of the SM and an active-power imbalance is given by the swing equation:

$$2H \frac{d\omega_r}{dt} = P_m - P_e - K_d (\omega_r - \omega_s). \quad (19)$$

Here, H denotes the inertia constant in seconds, ω_r is the angular rotor frequency, ω_g the angular frequency of the grid voltage, P_e the electrical power injected to the grid and K_d the damping coefficient of the machine, with all quantities but H in pu. For a SM operating in a stable steady-state operating point, electrical and mechanical power must be equal. During a grid disturbance, the power imbalance in such a machine will be its inertial response $P_H = P_m - P_e$. Laplace-transforming and rearranging yields

$$\omega_r s = \frac{-P_H}{2H} - \frac{K_d}{2H} (\omega_r - \omega_s). \quad (20)$$

As the mechanical time constants are much higher than the electrical, the SM's electrical power P_e can be expressed in quasi-steady state as in (2), neglecting the resistances. Assuming a dq -coordinate frame that is aligned with the machine's back EMF results in

$$P_e = \frac{V_{EMF} V_s}{X} \sin(\theta_r - \theta_s) = -\frac{V_{EMF}}{X} V_s^q, \quad (21)$$

where V_s^q denotes the source voltage q -component, and X the sum of reactances between the back EMF and source voltage. In the SC case with $P_m = 0$, back EMF and grid voltage are aligned with each other in steady state and V_s^q is zero. A change in the grid voltage phase angle would result in a misalignment of the voltages and an active power $P_H = P_e$.

For small angle differences, this can be linearized as

$$P_H = \frac{V_{EMF} V_s}{X} (\theta_r - \theta_s) = \frac{V_{EMF} V_s}{X_s} (\omega_r - \omega_g), \quad (22)$$

using the angular frequency and phase angle relationships

$$\theta_r s = \omega_r \quad \text{and} \quad \theta_s s = \omega_s. \quad (23)$$

In most cases, the additional power and consequently angle difference due to inertial response is small, and the linearization creates only negligible deviations. Using the previous equation to rearrange (20) with the SM maximum transferable active power $P_{smax} = \frac{V_{EMF} V_s}{X}$ results in

$$\omega_r s = -\left(\frac{K_d}{2H P_{smax}} s + \frac{1}{2H} \right) P_H. \quad (24)$$

Equivalent behaviour can be established for the IEL. If the emulated inertial-power reference P_H is chosen as the input to the IEL's PI-regulator, the derivative of the loop's internal frequency is determined as

$$\omega_{vr} s = -(K_p s + K_i) P_H, \quad (25)$$

where ω_{vr} is the loop's frequency estimate and K_p and K_i the proportional and integral gain, respectively. P_H is given by

$$P_H = -\frac{V_c}{X_f} V_g^q, \quad (26)$$

with the PCC voltage q -component V_g^q in the coordinate system aligned with the IEL angle θ_{vr} , and the filter reactance X_f ⁵. This equation is the two-port equation formulated with the converter terminal and PCC voltage. The virtual back EMF is replaced with the converter terminal voltage because the virtual resistance can take values that are too high to be neglected, making the use of the simplified two-port equation inaccurate. The Thévenin source voltage V_s is replaced with the PCC voltage because the latter can be directly measured. The tracking behaviour of SM and IEL given in (24) and (25), respectively, can be related to each other to establish equivalent behavior with the following tuning:

$$K_i = \frac{\omega_b}{2H}, \quad K_p = \frac{\omega_b K_d}{2H P_{max}}, \quad \text{with} \quad P_{max} = \frac{V_c V_g}{X_f}. \quad (27)$$

This formulation assumes all quantities in the IEL are in pu with the exception of virtual angular frequency ω_{vr} and virtual rotor angle θ_{vr} , which is why the base angular frequency ω_b appears in both expressions. Thus, the integral gain of the IEL directly relates to the inertia constant of the SM behavior to be reproduced, while the proportional gain represents the damping. It should be noted that the inertial effect from the IEL and the APL are cumulative. This is due to the reason that the IEL's inertial effect is added to the active-power reference fed to the APL, while the APL's inertial effect manifests as a power control error, i.e. in addition to the loop's power reference. To achieve the desired total inertial effect, the APL's inertia constant should be subtracted from the total inertia constant to determine the inertia constant used for tuning the IEL. The first-order APL's inertial effect is, based on (8), (18), and (24), given as $H_{PC} = \omega_b P_{vmax} / (4\alpha_{PC}^2)$. In case a second-order APL is used, the IEL is tuned with the total inertia constant. In either case, the cumulative inertial effect will be equivalent to a SM with the same inertia constant.

To enable the controller to leave active-power saturation after extreme grid-frequency disturbances more quickly, the auxiliary PI-controller suggested in [37] is implemented in the IEL.

C. Selection of Damping

As mentioned above, the proportional gain relates to the damping of the inertial response from the IEL. The relation in (27) determines K_p if a specific SM damping coefficient is to be reproduced. In a SM, damping is linked to physical properties such as friction and typically associated with losses. In consequence, SMs are usually poorly damped. In the IEL, the damping does not imply any losses, which means it becomes an additional degree of freedom. Increased damping comes however with the downside of a slower response.

⁵Instead of V_c and X_f , V_{EMF} and X_v could be chosen instead. Here, the converter voltage and filter reactance are chosen to avoid the power coupling dynamics introduced by R_v and to couple the emulated inertia closer to the grid voltage.

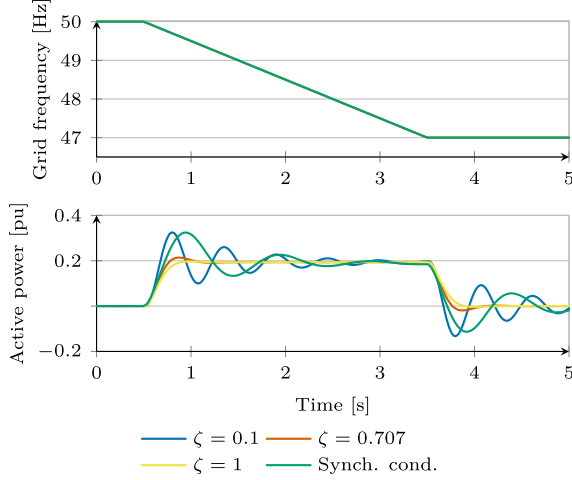


Fig. 7. Comparison with synchronous condenser and impact of the damping ratio on rise time and overshoot.

In the previous section was established that inertial response relates to tracking changes in the grid voltage angle with a specific speed. This tracking speed is determined by the IEL closed loop transfer function, given as

$$G_{IEL}(s) = \frac{\Delta\theta_{vr}}{\Delta\theta_g} = \frac{P_{\max}(K_p s + K_i)}{s^2 + P_{\max}K_p s + P_{\max}K_i}, \quad (28)$$

employing the small angle linearization

$$\Delta\theta_g = \frac{1}{V_g} \Delta V_g^q. \quad (29)$$

This is a damped second order response with a zero,

$$G_{IEL}(s) = \frac{2\zeta\omega_n s + \omega_n^2}{s^2 + 2\zeta\omega_n s + \omega_n^2}, \quad \text{where} \quad (30)$$

$$\omega_n = \sqrt{\frac{\omega_b P_{\max}}{2H}}, \quad \text{and} \quad \zeta = \sqrt{\frac{\omega_b}{2HP_{\max}}} K_d$$

using (27), which allows to determine the proportional gain based on the damping ratio as

$$K_p = \zeta \sqrt{\frac{2\omega_b}{HP_{\max}}}. \quad (31)$$

The effect of different damping ratios is shown in the results from time-domain simulations in Fig. 7. For this study case, the frequency of the voltage source is reduced with 1 Hz/s from 50 Hz to 47 Hz, while the steady-state active-power reference is set to $P_{\text{set}} = 0$ pu. The inertia constant is selected as $H = 4.68$ s, which together with the inertial contribution from the first-order APL employed in this simulation results in a total inertia constant of 5 s, meaning that the frequency disturbance should result in an inertial response of 0.2 pu. The figure demonstrates that the proposed controller is able to reproduce the behavior of a SM with good accuracy. The proposed approach combines a fast APL with a change in the power reference, while the response from the SM is purely based on its mechanical behavior. From the figure, it can be appreciated that the proposed solution has a smaller rise time when tuned to the same damping ratio as the

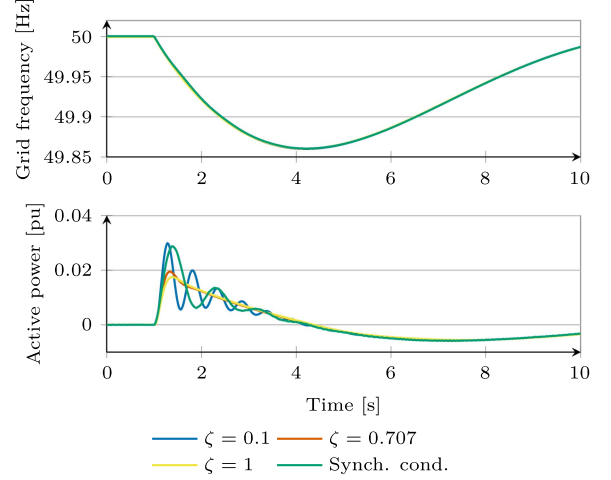


Fig. 8. Comparison of the inertial contribution from a synchronous condenser and an IEL with varying damping ratio during a frequency disturbance caused by a load step.

SM. This can be understood from (24), (25) and (27): As the filter reactance X_f used for the parameter selection in the IEL is smaller than a typical SM's transient reactance, the IEL's inertia is coupled more closely to the grid voltage and thereby reacts faster to frequency changes. It can also be seen that the low damping of the SM causes a challenging behavior. As the IEL damping can be freely adapted without any losses, a response without overshoot ($\zeta = 1$) can be selected. As an additional degree of freedom in the controller tuning, the damping ratio of the inertial response can be selected according to the needs and specifications of the converter system and the connecting grid. To achieve a compromise between speed and damping of the inertial response, a damping ratio of $\zeta = 0.707$ is suggested and chosen in this paper.

To study the impact of the damping of the inertial response under a more realistic grid frequency disturbance, a load step is simulated. The grid model employed is based on the lumped-mass representation of the Nordic synchronous area detailed in [38]. The lumped-mass model has a PID-governor and hydro-turbine model, which are tuned using the parameters given in [38]. The system model's ratings have been chosen in relation the size of the converter used for the experimental validation in Section IV, and are given in Table II in the appendix. The simulation results for a load step of 0.02 pu are shown in Fig. 8. As can be seen from the figure, the proposed controller can reproduce SM behaviour even for this disturbance type. Furthermore, the results show that increased damping does not have a notable effect on the frequency nadir.

D. Sequence Separation and Harmonic Filtering

Unbalanced conditions or operation under distorted grid voltages impact the IEL and result in an unsteady inertial-power reference. To avoid this, a sequence separation algorithm is applied to the PCC and converter-terminal voltages, as shown in Fig. 6. The RLS based method from [39] in its implementation in dq -coordinates as described in [25] is used here. As mentioned

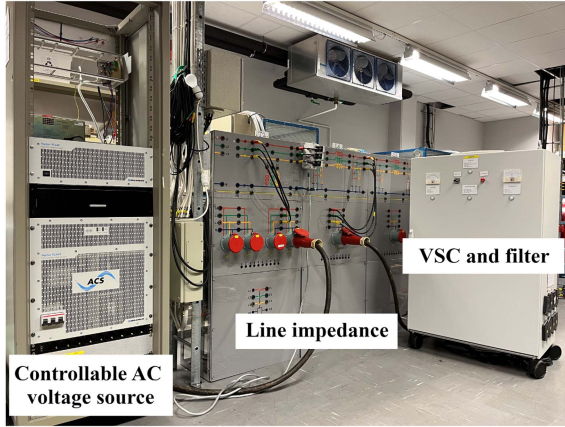


Fig. 9. Photo of the laboratory setup used for validation.

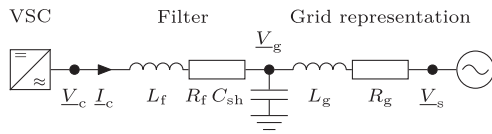


Fig. 10. Single-line diagram of the laboratory setup.

in [39], the method can be used to not only separate positive and negative sequences, but can in distorted grids also be used to simultaneously estimate selected harmonic components. The harmonics present in the grid voltage will lead to oscillations in $v_{g,q}$ in the IEL's reference frame, and are therefore added to the power reference by the IEL. Due to this, it can be advisable to use the RLS for harmonic estimation, in particular to the IEL's input signals, which allows to keep the active-power reference as free from harmonic content as possible. Due to the low-pass filtering characteristic of the RLS, the RLS provides some harmonic filtering even for the harmonics not explicitly included in the separation [39].

In this paper, for both the APL's and the IEL's RLS estimator the same relative bandwidth of $\xi = \omega_{RLS}/\omega_b = 0.9$ is selected to provide a good compromise between estimation time and estimation accuracy. In this paper, the IEL's estimator is tuned to provide sequence separation as well as harmonic estimation for 5th and 7th harmonic. The delay added by the RLS estimator has been shown to be negligible [24].

IV. EXPERIMENTAL VALIDATION

In this section the results of laboratory validation of the proposed controller are presented and discussed, verifying the effectiveness of the proposed solution in dealing with the challenges described in Section II. The experiments are conducted using the setup depicted in Fig. 9, which is illustrated in the single-line diagram in Fig. 10. In the laboratory setup, a REGATRON four-quadrant controllable AC power source is utilized to emulate the Thévenin voltage of the power grid, and inductors are used to adapt the grid strength according to $X_g = 1/SCR$. The GFM converter system is realized using a 2-level voltage source converter supplied by an ideal DC voltage source. The converter system is connected to the grid at the PCC through a

TABLE I
SYSTEM AND CONTROL PARAMETERS

System parameters		Control parameters	
S_N	1 kVA	L_{v1}	0.343 pu
V_N	100 V	R_{v1}	0.2343 pu
ω_b	314.16 rad/s	α_{PC}	2π 5 rad/s
L_f	0.157 pu	ζ_P	2
R_f	0.0157 pu	α_{CC}	2π 500 rad/s
SCR	3.18	α_{VC}	2π 1 rad/s
C_{sh}	0.0942 pu	H	5 s
		ζ	0.707

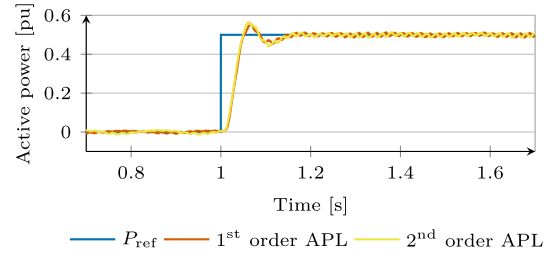


Fig. 11. Step response of the first- and second-order APL. Displayed is the positive-sequence active power.

filter reactor with inductance L_f and resistance R_f . A dSPACE DS1006 processor board is used to control the GFM converter. The setup's system and control parameters are given in Table I.

To validate the converter's response to a frequency disturbance, a linear frequency variation (frequency ramp) is considered, in accordance with [40], [41], [42]. A frequency ramp is the harshest condition for the synchronization system, as it leads to a constant phase variation (which depends on the ramp's slope). Furthermore, the use of a frequency ramp allows to directly verify that the inertia contribution corresponds to the desired inertia constant.

A. Comparison of Active-Power Loops

A step in the active-power reference is used to compare the performance of the first-order APL used in [24] and the second-order APL described in the previous section. At $t = 1$ s, the active-power reference is stepped from 0 to 0.5 pu. The IEL is deactivated during steps in the active-power reference to appreciate the dynamic performance of the APL. The results from this test are shown in Fig. 11. From the figure can be seen that the second-order APL's response in yellow is following the first-order APL's response in red. This shows that both APL designs provide equivalent reference tracking performance if the same closed-loop bandwidth is chosen due to the loop-shaping approach used to tune the controller parameters.

As explained, the reason to add a second-order integrator to the APL is to completely remove the APL's inertial response for constant RoCoFs. This effect is illustrated in Fig. 12, where the response of a first- and second-order APL to a frequency ramp of 5 Hz/s is shown. In both cases, the IEL is deactivated to emphasize the difference between the two APLs. As can be seen from the figure, the first-order APL provides an undesired inertial response during the RoCoF. In the second-order APL, the second-order integrator compensates for the constant RoCoF, removing

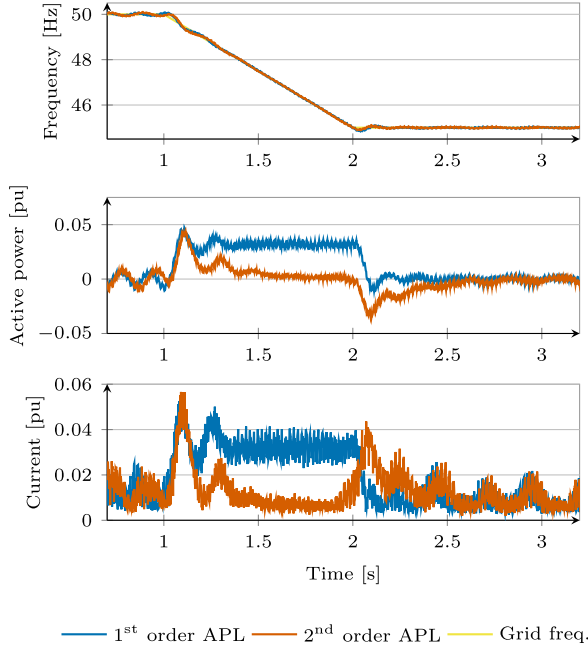


Fig. 12. Dynamic response of first- and second-order APL to a grid-frequency disturbance of 5 Hz/s during $t = 0$ s to 1 s. Top: Grid and internal converter frequency ($f_c = \omega_c/(2\pi)$). Middle: Positive sequence active power. Bottom: Converter-current magnitude I_c .

the inertial contribution after a short time. Even though the inertial contribution from the first-order APL may appear small in relation to the RoCoF, this power exceeds the active-power reference. In applications with limited energy storage such as a STATCOM, it is necessary to reduce the APL's inertia as much as possible to allow for tight control of the active-power exchange. Furthermore, as this inertial contribution is added onto the limited active-power reference, the injected power can exceed the limit if the reference saturates during a grid-frequency disturbance, to a lesser extent than but not unlike the integrated GFM.

B. Comparison With Integrated GFM

The proposed solution is here compared to an *integrated GFM* controller; as described in Section III, the latter consists of the first-order APL tuned to provide the same inertia and damping as the combined IEL and APL in the proposed solution. To compare the performance of the proposed solution to this controller, two experiments are conducted. In both cases the PCC-voltage is controlled by the converter to 1.0 pu, with an active-power reference of $P_{\text{set}} = 0.8$ pu. The first study case is a frequency reduction of the infinite voltage source, ω_s , from 50.0 Hz to 49.25 Hz at a rate of 0.5 Hz/s, while in the second case the frequency is varied with 2.0 Hz/s to a minimum of 47 Hz. In both cases, the disturbance has a duration of 1.5 s and begins at $t = 1$ s.

The results for the smaller RoCoF are shown in Fig. 13. From the figure it can be seen that the proposed GFM controller, plotted in red, is able to recreate the inertial response of the internal GFM controller in blue, with the only exception being a slightly larger overshoot at the beginning and end of the response. As

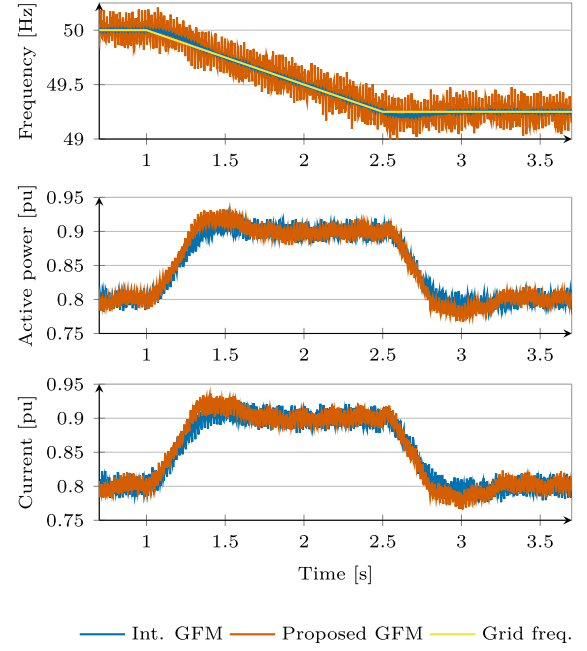


Fig. 13. Dynamic response of integrated GFM and proposed solution to a grid-frequency disturbance of 0.5 Hz/s during $t = 0$ s to 1.5 s. Top: Grid and internal converter frequency. Middle: Positive sequence active power. Bottom: Converter-current magnitude I_c .

the integrated GFM controller's provides inertia through a slow APL, the internal converter frequency ω_c is filtered in this case. Since the proposed controller's APL has a higher bandwidth, which comes with the advantages of improved synchronization and robustness as well as faster reference tracking, the converter frequency shows a higher harmonic content in this case. This increased harmonic content, however, does not result in more oscillations in the active power or current exchanged with the grid, as can be seen from the two lower plots showing active power and current. This experiment shows that the proposed control structure is able to recreate the inertial response of an integrated GFM or other VSM implementations.

Fig. 14 contains the results for the larger frequency disturbance. In this case the integrated GFM controller (blue) demonstrates the instability described in Section II: The current limiter prevents the power exchange to reach the necessary acceleration power, and the converter in consequence loses synchronism. The proposed GFM control structure shown in red is on the other hand able to limit the active-power exchange to 1 pu and maintains stable operation. It is important to stress that in the proposed solution, current limitation is purely achieved by the manipulation of the reference active-power signal and that the reference-current limiter (see Fig. 2) is never triggered. In contrast to the simulations presented in [24], the active power of the proposed solution does not exceed 1 pu and does immediately end when the RoCoF subsides. This is the result of the inclusion of the auxiliary PI controller described in [37].

C. Operation Under the Presence of Grid-Voltage Unbalance

The capability of the proposed solution to withstand unbalanced grid condition is tested in an experiment involving a

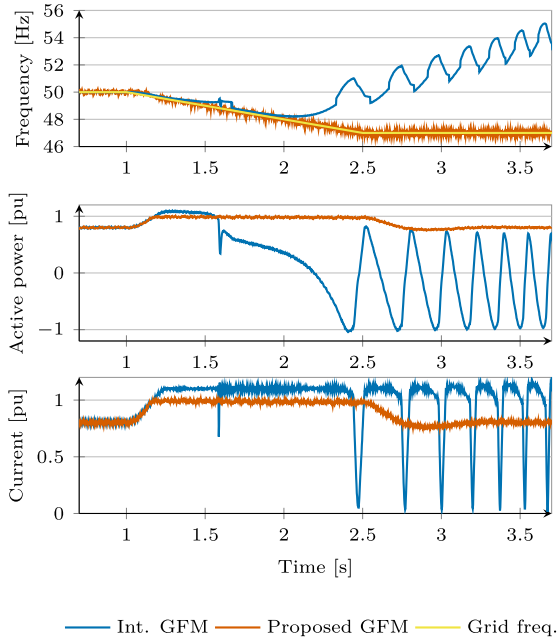


Fig. 14. Dynamic response of integrated GFM and proposed solution to a grid-frequency disturbance of 2 Hz/s during $t = 0$ s to 1.5 s. Top: Grid and internal converter frequency. Middle: Positive sequence active power. Bottom: Converter-current magnitude I_c .

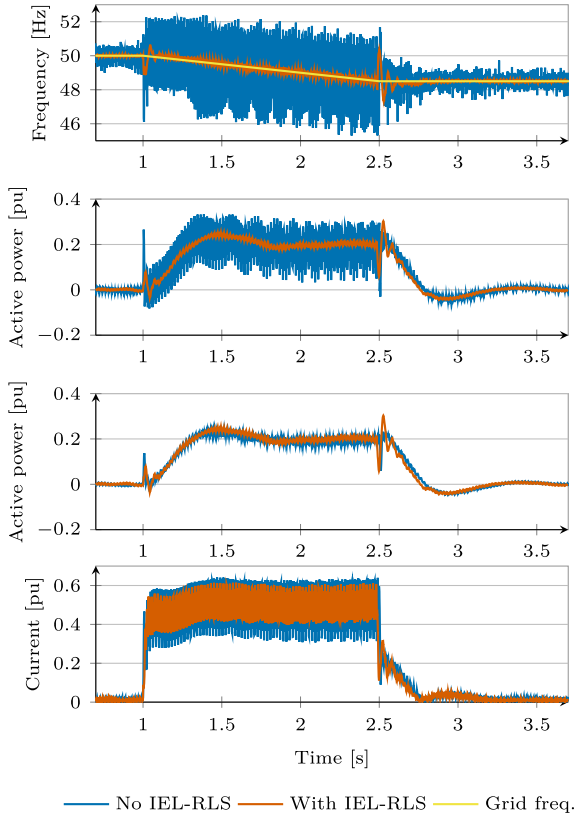


Fig. 15. Dynamic response of the proposed solution to a simultaneous single-phase voltage dip of 0.5 pu and grid-frequency disturbance of 1 Hz/s during $t = 0$ s to 1.5 s. From top to bottom: Grid and internal converter frequency, active power, positive-sequence active power, converter-current magnitude I_c .

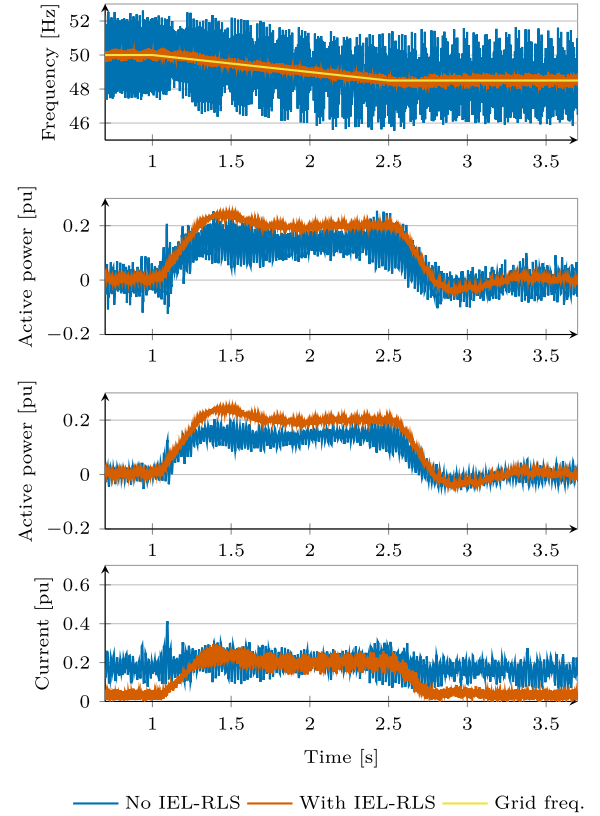


Fig. 16. Dynamic response of the proposed solution to a grid-frequency disturbance of 1 Hz/s during $t = 0$ s to 1.5 s under the presence of 5th- and 7th harmonic with a magnitude of 0.05 pu each. From top to bottom: Grid and internal converter frequency, active power, positive sequence active power, converter-current magnitude I_c .

single-phase voltage dip of 0.5 pu, together with a frequency disturbance of 1 Hz/s. This test also demonstrates the importance of sequence separation in the IEL. The results of the experiment are illustrated in Fig. 15, with the blue curves showing the results of deactivated sequence separation in the IEL, and the red curves the results of an active RLS providing sequence separation for the IEL. In both cases, the sequence separation for APL and current controller remains active.

As can be seen from the figure, without sequence separation the active power from the GFM is highly distorted. Without the sequence separation, the negative sequence causes a 100 Hz-oscillation in the dq -voltage vector, which is transferred into the voltage q -component and consequently to the inertial-power reference. The plot shows that there is even a notable amount of harmonic distortion before and after the disturbance, which is due to the unavoidable presence of unbalance and low-order harmonics in the laboratory setup. The addition of the RLS-based sequence separation in the IEL reduces the oscillations in the full active power drastically, and even removes most of the oscillations present in the positive-sequence active power. The small transient oscillations at the beginning and end of the fault are caused by the time needed for the RLS to correctly estimate the sequence components.

D. Operation Under the Presence of Grid-Voltage Harmonics

The IEL can not only cause oscillations in the active-power reference and active power exchanged with the grid when there are unbalances in the grid voltage, but also due to the presence of harmonics. This effect is demonstrated in the experiment shown in Fig. 16, where a 5th and 7th harmonic of 0.05 pu magnitude each are added to the grid voltage. As in the previous study, a grid-frequency disturbance of 1 Hz/s is applied for 1.5 s. Similar to the unbalanced case, the figure shows that the controller without filtering in the IEL (blue) causes more harmonic content in the active power. It can also be seen that this controller is not capable of providing the desired inertial response - this is due to the oscillation in the power reference exceeding the active-power limit. This saturation causes the active-power flow which is subjected to the filtering effect of the APL to have a reduced mean. The red curve, illustrating the controller with activated RLS estimator, shows reduced harmonic content in the power flows and the desired inertial response. If other harmonics are present in the intended application, they can similarly be removed by including them in the RLS estimation algorithm.

V. CONCLUSION

This paper has demonstrated that grid-frequency disturbances can be the cause of instability in inertia-providing GFM converters, and that the existing strategies to manipulate the power reference during current saturation are ineffective in this case. To solve the problem of loss of synchronism due to a slow active-power loop exposed to current limitation, a cascaded power controller consisting of an IEL in cascade with a fast APL has been proposed. A second-order integrator can be added to the APL to completely remove the APL's inertia. The experimental validation has confirmed that this approach effectively decouples the control elements responsible for provision of inertia and synchronization to the grid, resulting in a stable operation even during major disturbances. The proposed controller has been shown to be robust against unbalanced and distorted grid voltage conditions and to allow for effective active-power limitation while at the same time providing inertial support.

APPENDIX

TABLE II
LUMPED-MASS MODEL PARAMETERS FOR LOAD STEP SIMULATION

System parameters	
S_G	10 kVA
V_N	100 V
H_{sys}	5 s

REFERENCES

- [1] J. Matevosyan et al., "Grid-forming inverters: Are they the key for high renewable penetration?," *IEEE Power Energy Mag.*, vol. 17, no. 6, pp. 89–98, Nov.-Dec. 2019.
- [2] ENTSO-E, "High penetration of power electronic interfaced power sources and the potential contribution of grid forming converters," 2020. [Online]. Available: https://eepublicdownloads.entsoe.eu/clean-documents/Publications/SOC/High_Penetration_of_Power_Electronic_Interfaced_Power_Sources_and_the_Potential_Contribution_of_Grid_Forming_Converters.pdf
- [3] L. Huang, L. Zhang, H. Xin, Z. Wang, and D. Gan, "Current limiting leads to virtual power angle synchronous instability of droop-controlled converters," in *2016 IEEE Power Energy Soc. Gen. Meeting*, 2016, pp. 1–5.
- [4] B. Fan, T. Liu, F. Zhao, H. Wu, and X. Wang, "A review of current-limiting control of grid-forming inverters under symmetrical disturbances," *IEEE Open J. Power Electron.*, vol. 3, pp. 955–969, 2022.
- [5] M. G. Taul, X. Wang, P. Davari, and F. Blaabjerg, "Current limiting control with enhanced dynamics of grid-forming converters during fault conditions," *IEEE J. Emerg. Sel. Topics Power Electron.*, vol. 8, no. 2, pp. 1062–1073, Jun. 2020. [Online]. Available: <https://ieeexplore.ieee.org/document/8779657/>
- [6] E. Rokrok, T. Qoria, A. Bruyere, B. Francois, and X. Guillaud, "Transient stability assessment and enhancement of grid-forming converters embedding current reference saturation as current limiting strategy," *IEEE Trans. Power Syst.*, vol. 37, no. 2, pp. 1519–1531, Mar. 2022.
- [7] R. Rosso, S. Engelken, and M. Liserre, "On the implementation of an FRT strategy for grid-forming converters under symmetrical and asymmetrical grid faults," *IEEE Trans. Ind. Appl.*, vol. 57, no. 5, pp. 4385–4397, Sep.-Oct. 2021.
- [8] B. Wang, R. Burgos, and B. Wen, "Grid-forming inverter control strategy with improved fault ride through capability," in *2022 IEEE Energy Convers. Congr. Expo.*, 2022, pp. 1–8.
- [9] Y. Liu, H. Geng, M. Huang, and X. Zha, "Dynamic current limiting of grid-forming converters for transient synchronization stability enhancement," *IEEE Trans. Ind. Appl.*, vol. 60, no. 2, pp. 2238–2248, Mar.-Apr. 2024. [Online]. Available: <https://ieeexplore.ieee.org/document/10219024/>
- [10] T. Qoria, F. Gruson, F. Colas, G. Denis, T. Prevost, and X. Guillaud, "Critical clearing time determination and enhancement of grid-forming converters embedding virtual impedance as current limitation algorithm," *IEEE J. Emerg. Sel. Topics Power Electron.*, vol. 8, no. 2, pp. 1050–1061, Jun. 2020. [Online]. Available: <https://ieeexplore.ieee.org/document/8931732/>
- [11] Z. Yang, G. Zhao, and H. Yu, "Current limiting control method with adaptive virtual impedance for grid-forming STATCOM," *Energy Rep.*, vol. 9, pp. 453–460, 2023. [Online]. Available: <https://linkinghub.elsevier.com/retrieve/pii/S2352484723002603>
- [12] J. Erdocia, A. Urtaun, and L. Marroyo, "Dual voltage-current control to provide grid-forming inverters with current limiting capability," *IEEE J. Emerg. Sel. Topics Power Electron.*, vol. 10, no. 4, pp. 3950–3962, Aug. 2022. [Online]. Available: <https://ieeexplore.ieee.org/document/9641848/>
- [13] H. Lin, C. Jia, J. M. Guerrero, and J. C. Vasquez, "Angle stability analysis for voltage-controlled converters," *IEEE Trans. Ind. Electron.*, vol. 64, no. 8, pp. 6265–6275, Aug. 2017.
- [14] X. Wang, M. G. Taul, H. Wu, Y. Liao, F. Blaabjerg, and L. Harnefors, "Grid-synchronization stability of converter-based resources—An overview," *IEEE Open J. Ind. Appl.*, vol. 1, pp. 115–134, 2020.
- [15] Y. Geng, L. Zhu, X. Song, K. Wang, and X. Li, "A modified droop control for grid-connected inverters with improved stability in the fluctuation of grid frequency and voltage magnitude," *IEEE Access*, vol. 7, pp. 75658–75669, 2019.
- [16] L. Xiong, X. Liu, D. Zhang, and Y. Liu, "Rapid power compensation-based frequency response strategy for low-inertia power systems," *IEEE J. Emerg. Sel. Topics Power Electron.*, vol. 9, no. 4, pp. 4500–4513, Aug. 2021.
- [17] T. Qoria, X. Wang, and R. Kadri, "Grid-forming control VSC-based including current limitation and re-synchronization functions to deal with symmetrical and asymmetrical faults," *Electric Power Syst. Res.* vol. 223, 2023, Art. no. 109647. [Online]. Available: <https://linkinghub.elsevier.com/retrieve/pii/S0378779623005369>
- [18] L. Huang et al., "An adaptive inertia control to improve stability of virtual synchronous machines under various power grid strength," in *2019 IEEE Power Energy Soc. Gen. Meeting*, 2019, pp. 1–5.
- [19] Z.-L. Li, J. Hu, and K. W. Chan, "A new current limiting and overload protection strategy for droop-controlled voltage-source converters in islanded AC microgrids under grid faulted conditions," in *2020 IEEE Energy Convers. Congr. Expo.*, 2020, pp. 3888–3893.
- [20] L. Zhang, L. Harnefors, and H. Nee, "Power-synchronization control of grid-connected voltage-source converters," *IEEE Trans. Power Syst.*, vol. 25, no. 2, pp. 809–820, May 2010.
- [21] J. Chen, F. Prystupczuk, and T. O'Donnell, "Use of voltage limits for current limitations in grid-forming converters," *CSEE J. Power Energy Syst.*, vol. 6, no. 2, pp. 259–269, Jun. 2020.
- [22] A. Gkountaras, S. Dieckerhoff, and T. Sezi, "Evaluation of current limiting methods for grid forming inverters in medium voltage microgrids," in *2015 IEEE Energy Convers. Congr. Expo.*, 2015, pp. 1223–1230.

- [23] L. Huang, C. Wu, D. Zhou, and F. Blaabjerg, "A power-angle-based adaptive overcurrent protection scheme for grid-forming inverter under large grid disturbances," *IEEE Trans. Ind. Electron.*, vol. 70, no. 6, pp. 5927–5936, Jun. 2023.
- [24] P. Imgart, A. Narula, M. Bongiorno, M. Beza, and J. R. Svensson, "A cascaded power controller for robust frequency ride-through of grid-forming converters," in *2022 IEEE Energy Convers. Congr. Expo.*, 2022, pp. 1–8.
- [25] A. Narula et al., "Voltage-based current limitation strategy to preserve grid-forming properties under severe grid disturbances," *IEEE Open J. Power Electron.*, vol. 4, pp. 176–188, 2023.
- [26] M. Bongiorno, J. Svensson, and J.-P. Hasler, "A control system configured for, and a method for, emulating a virtual synchronous machine of a grid-forming voltage source converter," U.S. Patent WO/2024/074214, Apr. 11, 2024. [Online]. Available: https://patentscope.wipo.int/search/en/detail.jsf?docId=WO2024074214&_cid=P22-LVWK62-12618-1
- [27] J. Rocabert, A. Luna, F. Blaabjerg, and P. Rodríguez, "Control of power converters in AC microgrids," *IEEE Trans. Power Electron.*, vol. 27, no. 11, pp. 4734–4749, Nov. 2012.
- [28] R. Rosso, X. Wang, M. Liserre, X. Lu, and S. Engelken, "Grid-forming converters: Control approaches, grid-synchronization, and future trends – A review," *IEEE Open J. Ind. Appl.*, vol. 2, pp. 93–109, 2021. [Online]. Available: <https://ieeexplore.ieee.org/document/9408354/>
- [29] A. Narula, M. Bongiorno, M. Beza, and P. Chen, "Tuning and evaluation of grid-forming converters for grid-support," in *2021 23rd Eur. Conf. Power Electron. Appl.*, 2021, pp. P.1–P.10.
- [30] M. v. Wesenbeeck, S. d. Haan, P. Varela, and K. Visscher, "Grid tied converter with virtual kinetic storage," in *2009 IEEE Bucharest PowerTech*, 2009, pp. 1–7.
- [31] M. Schweizer, S. Almér, S. Pettersson, A. Merkert, V. Bergemann, and L. Harnefors, "Grid-forming vector current control," *IEEE Trans. Power Electron.*, vol. 37, no. 11, pp. 13091–13106, Nov. 2022.
- [32] A. Narula, M. Bongiorno, and M. Beza, "Comparison of grid-forming converter control strategies," in *2021 IEEE Energy Convers. Congr. Expo.*, 2021, pp. 361–368.
- [33] P. Rodríguez, I. Candela, C. Citro, J. Rocabert, and A. Luna, "Control of grid-connected power converters based on a virtual admittance control loop," in *2013 15th Eur. Conf. Power Electron. Appl.*, 2013, pp. 1–10.
- [34] A. Narula, M. Bongiorno, M. Beza, J. R. Svensson, X. Guillaud, and L. Harnefors, "Impact of steady-state grid-frequency deviations on the performance of grid-forming converter control strategies," in *2020 22nd Eur. Conf. Power Electron. Appl.*, 2020, pp. P.1–P.10. [Online]. Available: <https://ieeexplore.ieee.org/document/9215947/>
- [35] L. Harnefors, *Control of Variable Speed Drives*. Västerås Sweden: Mälardalen Univ., 2002.
- [36] P. Imgart, M. Beza, M. Bongiorno, and J. R. Svensson, "An overview of grid-connection requirements for converters and their impact on grid-forming control," in *2022 24th Eur. Conf. Power Electron. Appl.*, 2022, pp. 1–10.
- [37] P. Imgart, M. Bongiorno, J. R. Svensson, and M. Beza, "Stability limits and improved robustness of grid-forming converters with external inertia-emulation loop," in *2023 25th Eur. Conf. Power Electron. Appl.*, 2023, pp. 1–8. [Online]. Available: <https://ieeexplore.ieee.org/document/10264526/>
- [38] E. ENTSO-E et al., "Future system inertia 2," 2018. [Online]. Available: <https://docs.entsoe.eu/en/dataset/nordic-report-future-system-inertia/resource/6efce80b-2d87-48c0-b1fe-41b70f2e54e4>
- [39] M. Beza and M. Bongiorno, "Application of recursive least squares algorithm with variable forgetting factor for frequency component estimation in a generic input signal," *IEEE Trans. Ind. Appl.*, vol. 50, no. 2, pp. 1168–1176, Mar.-Apr. 2014.
- [40] Verband der Elektrotechnik Elektronik Informationstechnik e. V., "VDE FNN Guideline: Grid forming behaviour of HVDC systems and DC-connected PPMs," 2020. [Online]. Available: <https://www.vde-verlag.de/buecher/636341/grid-forming-behaviour-of-hvdc-systems-and-dc-connected-ppms.html>
- [41] Verband der Elektrotechnik Elektronik Informationstechnik e. V., "Technical requirements for grid connection of high voltage direct current systems and direct current-connected power park modules (VDE-AR-N 4131 TAR HVDC)," Mar. 2019. [Online]. Available: <https://www.vde-verlag.de/normen/0100511/vde-ar-n-4131-anwendungsregel-2019-03.html>
- [42] National Grid ESO, "Final modification report GC0137: Minimum specification required for provision of GB grid forming (GBGF) capability," 2021. [Online]. Available: <https://www.nationalgrideso.com/document/220511/download>



Paul Imgart (Graduate Student Member, IEEE) received the B.Sc. and M.Sc. degrees in power engineering from Leibniz University Hannover, Hannover, Germany. He is currently working toward the Ph.D. degree with the Chalmers University of Technology, Göteborg, Sweden. His work deals with the stability and robustness of sustainable power grids, with particular focus on innovative converter control strategies for converter-dominated systems.



Anant Narula (Member, IEEE) received the M.Sc. degree in smart electrical networks and systems (EIT InnoEnergy) from the KTH Royal Institute of Technology, Stockholm, Sweden, and Universitat Politècnica de Catalunya, Barcelona, Spain, in 2018, and the Ph.D. degree from the Chalmers University of Technology, Gothenburg, Sweden, in 2023. He is currently with Chalmers University of Technology as a postdoctoral Researcher for application of power electronics in power systems and stability studies of power system.



Massimo Bongiorno (Senior Member, IEEE) received the M.Sc. degree in electrical engineering from the University of Palermo, Palermo, Italy, in 2002, and the Lic. Eng. and Ph.D. degrees in electric power engineering from the Chalmers University of Technology, Gothenburg, Sweden, in 2004 and 2007, respectively. From 2007 to 2010, he was an Assistant Professor with the Department of Electric Power Engineering, Chalmers University of Technology, where he became an Associate Professor in 2010. Since 2015, he has been holding the position of a Professor in power electronic applications for power systems and since 2020 he has been the Head of the Division of Electric Power Engineering, Chalmers University of Technology. His research interests include the application of power electronics in power systems, converter control, power system dynamics, and power quality.



Mebtu Beza (Member, IEEE) received the B.Sc. degree in electrical engineering from Bahir Dar University, Bahir Dar, Ethiopia in July 2005, and the M.Sc., Lic.Eng., and Ph.D. degrees in electric power engineering from the Chalmers University of Technology, Gothenburg, Sweden, in 2009, 2012, and 2015, respectively, and the D.Sc. degree (Docent) in control and modeling of power electronic converters in power systems from the Chalmers University of Technology, in 2020. He is currently an Associate Professor with the Chalmers University of Technology. His research interests include signal processing in power systems, control theory, stability studies in converter-dominated systems, converter topologies and application of power electronics in power systems.



Jan R. Svensson (Senior Member, IEEE) received the Ph.D. and D.Sc. degrees (Docent) in electric power engineering from the Chalmers University of Technology, Göteborg, Sweden, in 1988 and 2002 respectively. From 1999 to 2009, he was with ABB in R&D of HVDC Transmission, STATCOMs, and energy storages, especially design and control of light-concept devices (HVDC and FACTS). Between 2009 and 2014, he was the Program Manager for the Global R&D Program "Active Grid Infrastructure" with ABB Corporate Research. From 2014 to 2020,

he was a Senior Principal Scientist on power electronics systems with ABB Power Grids Research. In addition to his current role as a Research Fellow with Hitachi Energy Research, Västerås, Sweden. He has also been an Adjunct Professor with Chalmers University of Technology since 2018. His research interests include design and control of power electronics in power systems, power quality, storage technologies, and renewable energy.